Interfacially Modified Si-Pd/Carbon Catalyst for Selective Pulegone (C=C bond) Hydrogenation to Menthone–Isomenthone

Prashant Kumar Thakur,[abc] Priyabrat Mohapatra,[d] Chandan Singh Chanotiya,[ab] Bhavana R. Shivankar,[be] Andrew Hung,[e] Ylias Sabri,*[c] Prasant kumar Rout *[ab]

[a]*Phytochemistry Division, CSIR-Central Institute of Medicinal and Aromatic Plants, Lucknow 226015, Uttar Pradesh, India*

[b]*Academy of Scientific and Innovative Research (AcSIR), New Delhi-110025, India.*

[c]*Department of Chemical and Environmental Engineering, RMIT University, Melbourne 3001, Australia.*

[d]*Department of Chemistry, Krupajal Engineering College, Bhubaneswar, Odisha 751002, India*

[e]School of Science, STEM College, *RMIT University, Melbourne 3001, Australia.*

Corresponding authors

Dr. PK Rout (Scientist-F & Professor)

Email: pkrout.cimap@csir.res.in

Dr. Ylias Sabri (Associate Professor)

Email: Ylias.sabri@rmit.edu.au

Table of content:

Fig.S13: Projected density of states (PDOS) of (a) Pd-C and (b) Si-Pd-C surfaces, and of pulegone adsorbed through C=O and C=C motifs on Pd-C [(c,d)] and Si-Pd-C [(e,f)], illustrating the influence of Si incorporation on electronic structure and adsorbate-surface interactions.
Fig: S14. Charge density difference (CDD) plots for pulegone adsorption on Pd-C surfaces showing (a) C=C and (b) C=O binding configurations, and on Si-Pd-C surfaces showing (c) C=C and (d) C=O binding configurations (isovalue = 0.01 e $bohr^{-3}$). Yellow and cyan isosurfaces represent charge accumulation and charge depletion, respectively.

List of Tables

1. Materials and catalyst preparation

1.1. Materials

Palladium nitrate dihydrate ($Pd(NO_3)_2 \cdot 2H_2O$), nickel nitrate hexahydrate ($Ni(NO_3)_2 \cdot 6H_2O$), ruthenium nitrosyl nitrate ($Ru(NO)(NO_3)_3$), tetraammineplatinum(II) nitrate ($Pt(NH_3)_4(NO_3)_2$), tetraethyl orthosilicate (TEOS), sodium carbonate (Na_2CO_3), and activated carbon (AC) were purchased from Sigma-Aldrich and used as received without further purification. Deionised water was used in all synthesis procedures.

Pulegone (analytical grade) was purchased from Sigma-Aldrich. Dementholised oil (DMO) and *CIM-Vishisht* essential oil were obtained from steam distillation of *Mentha arvensis* (*CIM-Vishisht* variety) cultivated at the CSIR-CIMAP experimental farm. DMO was collected after separation of menthol from *Mentha arvensis* essential oil via fractional crystallisation.

1.2. Preparation of catalyst

Synthesis of Si-Pd/C catalyst

Si-Pd/C catalysts were prepared via a deposition–precipitation/sol–gel hybrid route. $Pd(NO_3)_2 \cdot 2H_2O$ was dissolved in deionised water and heated to 60 °C under stirring, followed by dropwise addition of Na_2CO_3 to adjust pH to 9 to form $Pd(OH)_2$/basic Pd carbonate species. In parallel, TEOS was dissolved in ethanol and added to the Pd suspension; under alkaline aqueous–alcoholic conditions, TEOS underwent in situ hydrolysis and condensation, generating SiO_x species that deposited onto the carbon surface and promoted Pd–O–Si interfacial environments. Activated carbon was then introduced and the slurry was stirred for 2 h, filtered, washed thoroughly with water, dried at 120 °C for 12 h, and calcined at 650 °C for 4 h (5 °C min^{-1}). Si loading was varied (3–7 wt%) at constant Pd loading (2 wt%), giving 3%Si–2%Pd/AC, 5%Si–2%Pd/AC, and 7%Si–2%Pd/AC.

Benchmark catalysts (5%Ni/C, 5%Ni–SiO_2, 5%Pd/SiO_2, 5%Pt/C, and 5%Ru/C) were synthesised using an identical deposition–precipitation protocol to ensure fair comparison. The corresponding nitrate precursors ($Ni(NO_3)_2 \cdot 6H_2O$, $Pd(NO_3)_2 \cdot 2H_2O$, $Pt(NH_3)_4(NO_3)_2$, and $Ru(NO)(NO_3)_3$; Sigma-Aldrich) were dissolved in deionised water and stirred at 60 °C. The pH was adjusted to 9 by dropwise addition of Na_2CO_3, forming the respective metal hydroxide or basic carbonate species in situ. Activated carbon or commercial SiO_2 was then added as the support, and the suspension was stirred for 2 h to allow uniform deposition of the metal species onto the support surface. The resulting solids were filtered, washed thoroughly with deionised water, dried at 120 °C for 12 h, and calcined at 650 °C for 4 h (heating rate 5 °C min^{-1}). This consistent preparation and activation strategy ensures that observed differences in catalytic performance arise from intrinsic metal–support interactions rather than synthetic artefacts.

2. Characterization of catalysts

The XRD spectra of the composites were recorded through Rigaku diffractometer (Rigaku, Japan) by using Cu Kα radiation at 40 kV and 130 mA in the scanning angle of 5-90^o at 0.05^o scanning speed. The spectra are presented with the Intensity Vs 2θ. FT-IR spectra of the samples were acquired using Nicolet 138 400D-Impact FT-IR spectrophotometer. After applying 10,000 psi hydraulic pressure for 2-3 min, the dry KBr (200 mg) and the sample of 5 mg were well mixed to create pellets. It was analyzed between 4000-500 cm^{-1} at a resolution of 4 cm^{-1}. Each sample was scanned 200 times, and the wave number against transmittance (%) was used for recording the spectra. Thermogravimetric analysis (TGA) of the quartz filters was performed using a Mettler-Toledo TGA/DSC 1 STAR system. Approximately 5 mg of sample was placed in a silica crucible and analysed under the following temperature program: 30-800 ^{o}C at a heating rate of 10 °C min^{-1}, with nitrogen used as the purge gas at a flow rate of 40 mL min^{-1}. The obtained data were examined after obtaining the first derivative (DTG) to ensure an unambiguous interpretation. The QUANTA-250, FEI (Netherlands) SEM equipment was utilized to conduct a morphological study of the synthesized catalysts. Samples (50 mg) were coated with gold by Sputter Coater for 50 s (Model 147, No. Q150 TES Frocoram Technology, U.K). Sputtering with gold was used to create layers on the materials. The instrument was kept at 30 kV to determine the particle size and shape of the materials. X-ray photoelectron spectroscopy (XPS) was carried out using a Thermo Scientific K-Alpha instrument with monochromatic Al Kα radiation (E_photon = 1486.6 eV). Binding energy

(B.E.) corrections were applied using the C 1s peak at 284.8 eV as an internal standard for both core levels and valence band maxima. Surface area measurements were obtained by the Brunauer-Emmett-Teller (BET) method, and the pore volume and pore size were determined using the Barrett-Joyner-Halenda (BJH) method. These values were assessed through nitrogen (N_2) adsorption-desorption isotherms on a BEL Sorb II instrument (Japan) at liquid nitrogen temperature. Before testing, the samples underwent degassing at 110°C for 5 hours. BET analysis was then performed overnight in a liquid nitrogen environment. TEM was performed by using an electron microscope with a filament as a source of electrons operated at 300 kV. TEM imaging and mapping were carried out by using Field Emission Gun-Transmission Electron Microscope 300 kV (TEM 300 kV), FEI, Tecnai G2, F30. High-resolution transmission electron microscopy (HR-TEM) imaging was conducted at 200 kV using a JEOL 2010 microscope to capture detailed material morphologies.

3. Reaction conditions

The synthesized catalysts were evaluated for the semi-synthesis of thymol and menthone/isomenthone from pulegone. The procedure involved loading of pulegone in an organic solvent (ethanol) into a 25 mL pressurized reactor (in-house designed glass reactor) as outlined in Scheme S1. Subsequently, the catalyst was added to the solution at a pre-determined ratio. The reaction mixture was then agitated within a temperature range of 40-90 °C for 30-90 min under varying hydrogen (H_2) pressure ranging from 2 to 50 psi depending on the desired product selectivity. Upon completion, the reaction solution was filtered, and stored at moderate temperature for subsequent analysis. The samples were analyzed by GC-FID and GC/MS. Following each batch reaction, the recovered catalysts were subjected to washing with water and calcination to regenerate their activity, ensuring their reusability for at least the subsequent five batch processes. The schematic representation of targeted products and formation of possible side products during pulegone transformation is listed in Fig. 1.

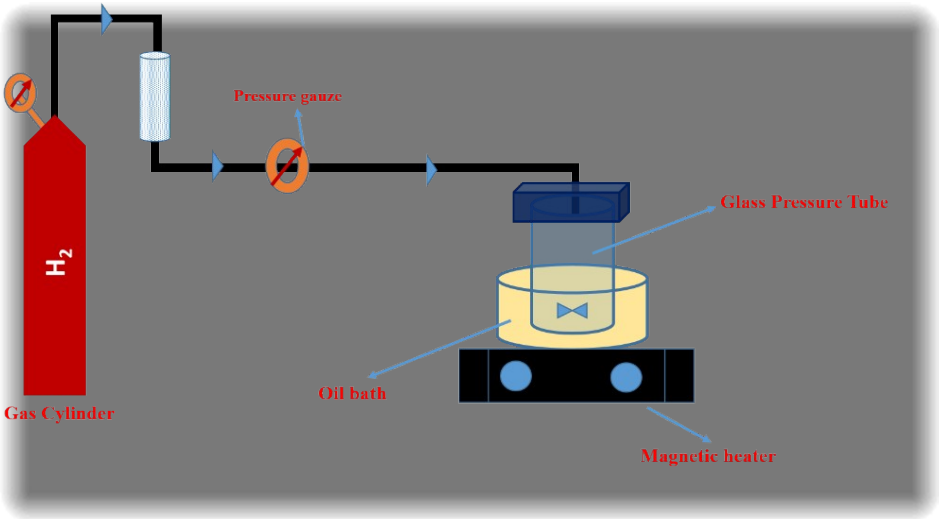

Scheme S1. Schematic design of lab customised glass tube reactor for low pressure reaction operations.

4. Experimental design

RSM serves as an advanced design tool for experiments, enabling the identification of optimal variable levels to enhance the response. Within RSM, the BBD stands out as a response surface design that predicts both first and second-order coefficients. These designs belong to a class of rotatable quadratic designs based on three-level incomplete factorial designs. BBD was employed in this study to assess the impact of various process factors on the response. The acceptance of the generated process optimization model relies on the estimation of coefficients, outcome prediction, and the alignment of other variables with Eq. S1

$Y= f (X_1, X_2$----------$X_n) \pm E$ ----------Eq. S1

Here Y; response, f; response function, X_1-X_n; independent variables, E; investigational error Polynomial quadratic model is represented in Eq. S2. F is influenced by the independent variables and Eq. S2 outcome.

$$Y = \beta_0 + \sum_{i=1}^{n} \beta_i X_i + \sum_{i=1}^{n} \beta_{ii} X_i^2 + \sum_{i=1}^{n-1} \sum_{j=i+1}^{n} \beta_{ij} X_i X_j + E \quad \text{----------Eq. S2}$$

Here Y; anticipated response, β_0; regression co-efficient, β_i, β_{ii}, and β_{ij}; linear, quadratic and interaction co-efficient, Xi and Xj; processed variables coded values, E; experimental/ residual error.

In the specific application of BBD, three independent variables - temperature, pressure, and reaction time were examined for their effects on two reactions: pulegone to thymol and menthone/isomenthone. The goal was to achieve the highest yield percentage. For thymol synthesis, the temperature (50-90 ˚C), H_2 pressure (10-50 psi), and reaction time (30-90 min) were varied. On the other hand, the temperature (40-60 ˚C), H_2 pressure (2-10 psi), and reaction time (30-60 min) were manipulated for the synthesis of menthone/isomenthone. Experiments were designed at three levels (-1, 0, and +1), as detailed in Table S1. Finally, 2D contour plots and 3D surface representations of the observed response surface were developed to establish the optimum conditions.

Table S1. Parameter level and coded values for thymol and menthone/isomenthone semisynthesis used in the Box Behnken design.

Variables	Symbol	Coded levels for Menthone/Isomenthone		
		-1	**0**	**+1**
Temperature (^oC)	A	40	50	60
H_2 pressure (PSI)	B	2	6	10
Reaction time (min)	C	30	45	60

5. TGA analysis of synthesized materials

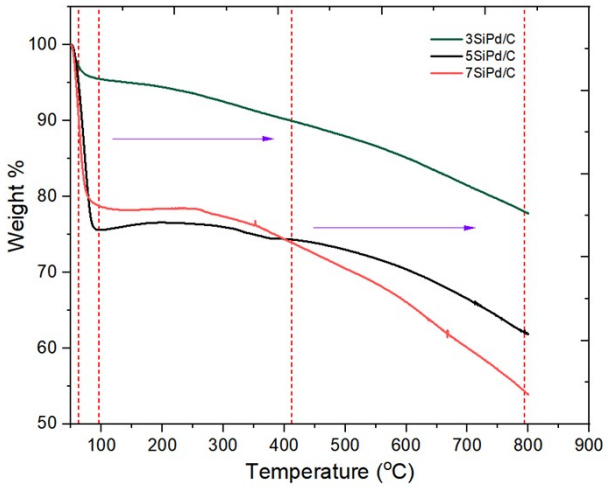

Fig. S1: TGA spectra of Si modified Pd/C catalysts

6. Surface Area analysis of 5%Si-Pd/C catalyst

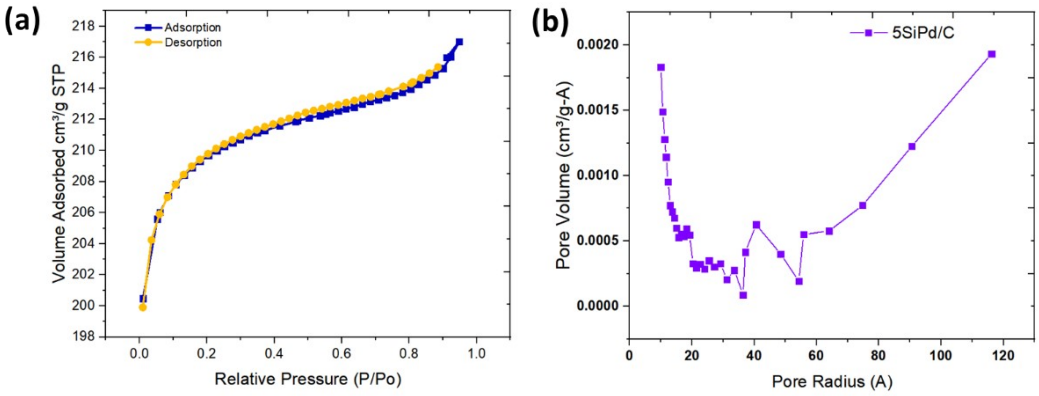

Fig. S2: Surface area (a) and pore radius (b) plot of 5%Si-Pd/C catalyst.

Table S2. Surface area analysis of synthesized materials.

Catalyst	BET Surface area (m^2/g)	Avg. pore radius (nm)	Pore volume (cm^3/g)
5%Si-Pd/C	626.26	14.81	0.30
5%Pd/C	712.64	13.94	0.25

7. XPS analysis of synthesized materials

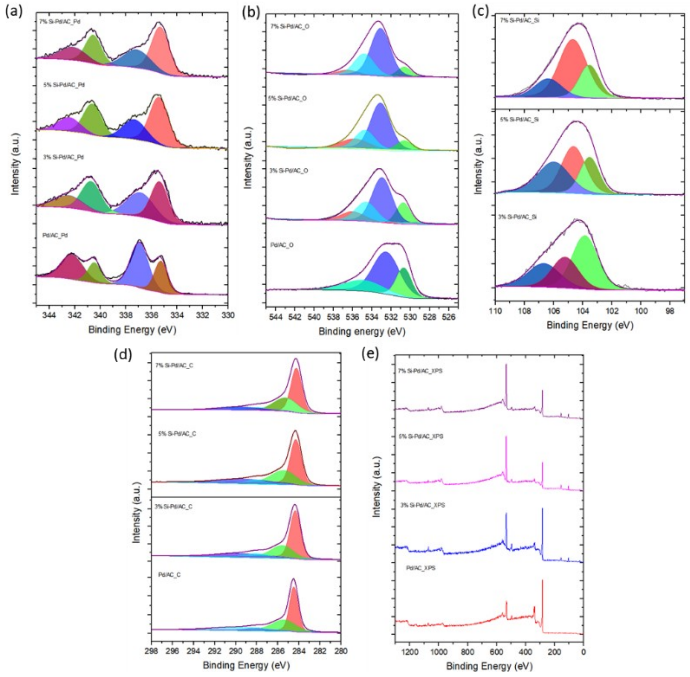

Fig. S3: High-resolution XPS spectra of (a) Pd 3d, (b) O 1s, (c) Si 2p, and (d) C 1s regions for Pd/C and Si-modified Pd/C catalysts, showing Si-content-dependent modulation of Pd electronic states and the presence of Si-O-C interfacial domains. (e) Wide-scan XPS spectra confirming elemental composition.

To quantitatively elucidate the effect of Si incorporation on the Pd electronic state, the Pd 3d XPS spectra were deconvoluted and the relative fractions of Pd^0 and Pd^{2+} were determined for all catalysts (Table S3, Fig. S3). The parent 5%Pd/C catalyst contains a high proportion of oxidised Pd^{2+} species (66.03%), with a low Pd^0/Pd^{2+} ratio of 0.51, indicating limited electron density at Pd sites. Upon Si incorporation, a pronounced increase in metallic Pd^0 fraction is observed. The Pd^0/Pd^{2+} ratio increases to 1.28 for 3%Si-Pd/C and reaches a maximum value of 1.82 for 5%Si-Pd/C, demonstrating optimal electronic modulation of Pd via Si-O-Pd interfacial interactions. Further increasing Si loading to 7% results in a slight decrease in the Pd^0/Pd^{2+} ratio (1.52), suggesting partial over-coordination of Pd by SiO_x species.

This non-monotonic trend directly correlates with the catalytic performance, where 5%Si-Pd/C exhibits the highest menthone/isomenthone selectivity. The results confirm that Si does not merely enhance Pd dispersion, but quantitatively tunes the Pd electronic structure through Pd-O–Si-C interfacial motifs, optimizing hydrogen activation and suppressing carbonyl over-hydrogenation. These findings strengthen the mechanistic basis of the proposed Si-Pd interfacial synergism.

Table S3 Effect of Si content on Pd electronic state

Catalyst	Pd^0 (%)	Pd^{2+} (%)	Pd^0/Pd^{2+}

Catalyst	Pd^0 (%)	Pd^{2+} (%)	Pd^0/Pd^{2+}
5%Pd/C	33.97	66.03	0.51
3%Si-Pd/C	56.03	43.7	1.28
5%Si-Pd/C	63.56	34.91	1.82
7%Si-Pd/C	60.08	39.92	1.52

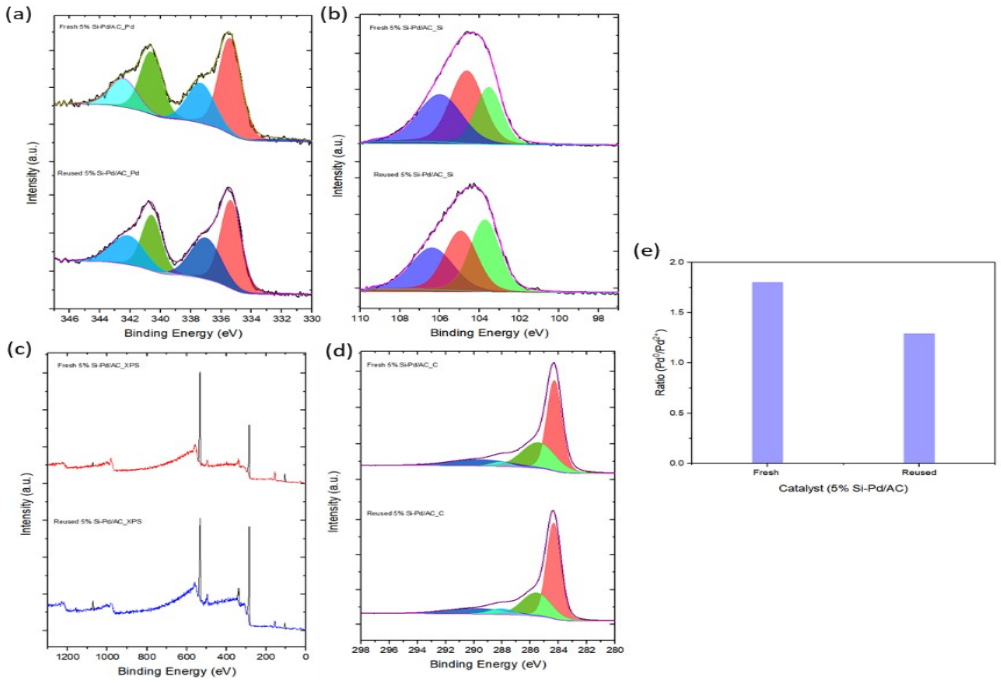

Fig. S4: XPS analysis of fresh and reused 5%Si-Pd/C catalyst after five catalytic cycles. High-resolution spectra of (a) Pd 3d, (b) Si 2p, and (d) C 1s regions showing preservation of Pd electronic states and Si-O-C interfacial environments after reuse. (c) Corresponding wide-scan XPS spectra confirming the elemental integrity of the catalyst. (e) Comparison of Pd^0/Pd^{2+} ratios for fresh and reused catalysts, indicating only minor electronic changes and confirming excellent interfacial and chemical stability upon recycling.

8. TEM Reused Material

TEM analysis of the reused 5%Si-Pd/C catalyst (Fig. S5a) reveals that Pd nanoparticles remain well anchored on the carbon support after five catalytic cycles, with no evidence of large-scale aggregation or particle detachment. The corresponding particle size distribution (Fig. S5b) shows a unimodal profile centered at approximately 11-13 nm, representing a moderate increase relative to the fresh catalyst (≈5-7 nm). This modest particle growth is attributed to limited Pd sintering during repeated thermal regeneration at 450 °C, rather than catalyst

deactivation or structural collapse. Importantly, the absence of broad tails at larger sizes (>20 nm) indicates that Si incorporation effectively suppresses severe sintering, consistent with strong Pd-O-Si-C interfacial interactions. These observations correlate well with the minimal loss in catalytic activity and selectivity (~4-5%) observed during reusability tests, confirming that the Si-modified support stabilizes Pd nanoparticles and preserves active-site integrity under prolonged reaction conditions.

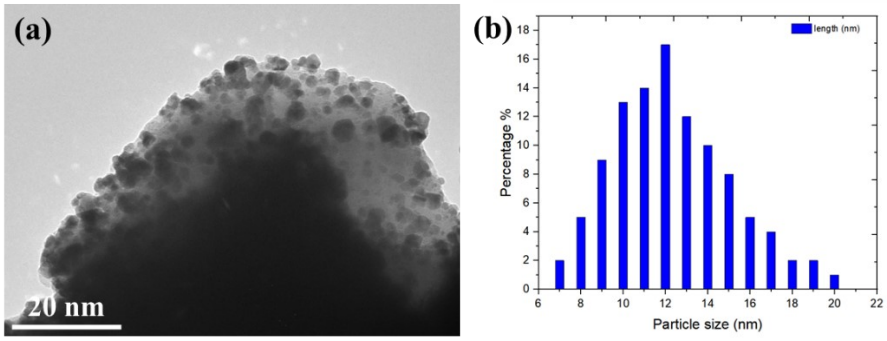

Fig. S5. (a) TEM image of the reused 5%Si-Pd/C catalyst after five consecutive hydrogenation cycles, showing Pd nanoparticles retained on the carbon matrix; (b) corresponding particle size distribution histogram derived from TEM analysis, indicating a narrow distribution centered at ~11-13 nm**.**

9. Material screening and reaction parameter optimization

Table S4: material screening and optimization

Catalysts	Conversion%	Catalyst dosage (Wt. %)	Menthone/Isomenthone	Menthol	Isopulegol
5%Pd/C	93	10	55.2	42.1	1.6
3% Si-2%Pd/C	92	10	78.2	15.2	1.2
5%Si-2%Pd/C	95	10	89.3	7.2	3.1
7%Si-2%Pd/C	96	10	88.6	6.3	3.4
5%Si-2%Pd/C	98	15	74.7	14.9	6.2
5%Ni-SiO_2	94	10	27.8	55.8	4.8
5%Pd/SiO_2	91	10	44.5	49.3	1.8
5%Pt/C	92	10	38.6	65.7	0.5

5%Ni/C	95	10	42.4	52.6	2.1
5%Ru/C	90	10	48.7	47.8	3.3

Operating conditions (1 mmol pulegone, 60 °C, 10 psi H_2, 55 min, 10 wt% catalyst)

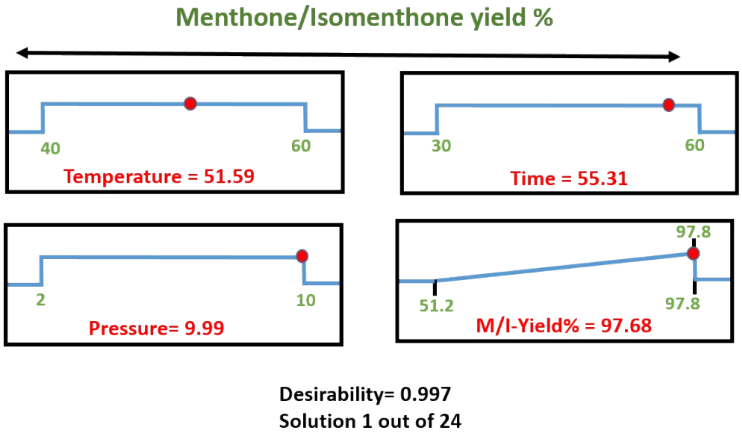

Fig. S6: Optimized parameters obtained from RSM-BBD module for Menthone/ isomenthone yield.

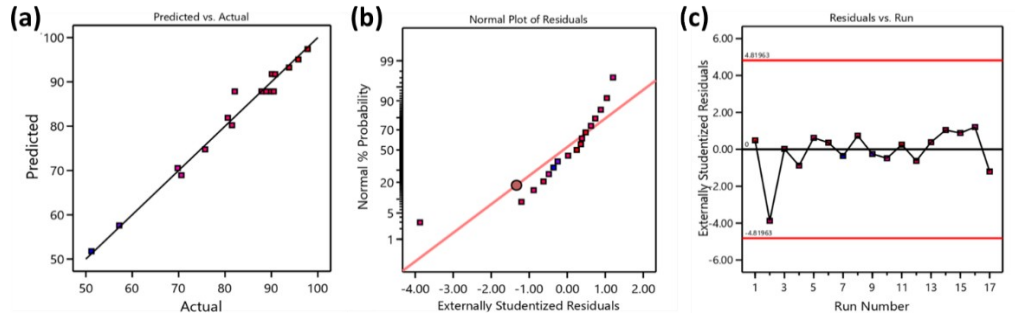

Fig. S7: Relationship between actual and predicted value (a,b), internally studentized residual plot Menthone/Isomenthone yield (c).

Table S5 summarizes the Box–Behnken Design (BBD) employed to evaluate the combined effects of temperature (40-60 °C), H_2 pressure (2-10 psi), and reaction time (30–60 min) on menthone/isomenthone yield over the 5%Si–Pd/C catalyst, while maintaining constant substrate loading (1 mmol pulegone) and catalyst dosage (10 wt%). The BBD consists of 17 experimental runs, including 12 edge points and 5 centre-point replicates (50 °C, 6 psi H_2, 45 min), which were intentionally incorporated to estimate experimental error, assess reproducibility, and validate model robustness. The centre-point experiments were performed independently under identical conditions to evaluate process variability. Minor deviations among these replicates are expected due to experimental uncertainties inherent to batch hydrogenation reactions, such as gas–liquid mass transfer, catalyst wetting, and

sampling. One replicate (Run 1) showed a comparatively lower yield; however, statistical analysis (ANOVA and residual diagnostics Table S7) confirmed that this data point falls within acceptable confidence limits and does not distort the fitted quadratic model. No data were excluded, and all centre-point runs were retained to preserve statistical integrity.

Table S5. Experiment design of BBD matrix using 5%Si-Pd/C catalyst.

Run	Temperature (^oC)	H_2 Pressure (psi)	Time (min)	Menthone/Isomenthone Yield (%)
C1	50	6	45	82.1
C2	50	6	45	87.9
C3	50	6	45	90.5
C4	50	6	45	89.8
C5	50	6	45	88.9
E1	60	6	30	80.6
E2	50	2	30	57.2
E3	50	2	60	69.8
E4	60	6	60	90.8
E5	50	10	60	97.8
E6	50	10	30	95.8
E7	40	6	60	81.5
E8	40	10	45	90.1
E9	40	6	30	75.7
E10	40	2	45	51.2
E11	60	10	45	93.8
E12	60	2	45	70.6

Fixed parameters: 1 mmol pulegone, 10 wt% catalyst, C1-C5: Centre Points, E1-12: Edge Points.

In addition, to confirm the reproducibility of the optimization outcome, the predicted optimum reaction conditions were experimentally validated by five independent runs. The resulting yields were highly consistent and are reported in Table S6, demonstrating excellent reproducibility of the optimized conditions. These additions improve clarity and further support the robustness of the optimization and conclusions.

Table S6: Reproducibility test of optimum reaction parameters obtained from BBD matrix.

Runs	H_2 pressure (PSI)	Reaction time (min)	Temperature (^oC)	Yield % [a]
1	10	55	50	97.6
2	10	55	50	97.4
3	10	55	50	97.6
4	10	55	50	97.7
5	10	55	50	97.5

[a] 1 mmol Pulegone, 10 wt% catalyst loading.

Experimental design and data handling of RSM-BBD Matrix

A Box–Behnken Design (BBD) was employed to evaluate the effects of temperature (40-60 °C), hydrogen pressure (2-10 psi), and reaction time (30-60 min) on menthone/isomenthone yield using 5%Si-Pd/C as catalyst. The design consisted of twelve edge points and five centre-point replicates (50 °C, 6 psi, 45 min), which were included to estimate pure experimental error and assess process reproducibility. All experiments were conducted independently under identical fixed parameters (1 mmol pulegone, 10 wt% catalyst). Variations observed among centre-point replicates reflect normal batch-to-batch experimental variability typical of low-pressure hydrogenation reactions. No data points were excluded or treated as outliers; all results were retained for response-surface model fitting and statistical analysis.

Table S7 Statistical summary of different models for menthone/isomenthone synthesis

Source	Std. Dev.	R^2	Adjusted R^2	Predicted R^2	PRESS	
Linear	5.95	0.8367	0.7990	0.7317	757.18	
2FI	6.05	0.8702	0.7923	0.6388	1019.35	
Quadratic	**2.87**	**0.9796**	**0.9533**	**0.9032**	**273.14**	**Suggested**
Cubic	3.35	0.9841	0.9362	-	*	Aliased

Table S8 ANOVA data of menthone/isomenthone yield (quadratic module)

Source	Sum of Squares	df	Mean Square	*F*-value	p-value	
Model	2764.60	9	307.18	37.29	< 0.0001	significant
A-Temperature	173.91	1	173.91	21.11	0.0025	

B-Time	117.05	1	117.05	14.21	0.0070	
C-Pressure	2070.46	1	2070.46	251.32	< 0.0001	
AB	4.84	1	4.84	0.5875	0.4684	
AC	61.62	1	61.62	7.48	0.0291	
BC	28.09	1	28.09	3.41	0.1073	
A^2	93.31	1	93.31	11.33	0.0120	
B^2	4.06	1	4.06	0.4933	0.5051	
C^2	189.43	1	189.43	22.99	0.0020	
Residual	57.67	7	8.24			
Lack of Fit	12.68	3	4.23	0.3757	0.7763	not significant
Pure Error	44.99	4	11.25			
Cor Total	2822.27	16				

Table S9. Fit statistics of Menthone/Isomenthone yield%.

Menthone/ Isomenthone yield %			
Std. Dev.	2.87	**R^2**	0.9796
Mean	82.01	**Adjusted R^2**	0.9533
C.V. %	3.50	**Predicted R^2**	0.9032
		Adeq Precision	20.7425

10. Kinetic and durability study

The dehydrogenation and reduction processes involved in pulegone transformation are inherently intricate to lead various side products. To gain a comprehensive understanding of the catalytic conversion process, a kinetic study was conducted focusing on composites (2%Pd-3%Si/C). The investigation aimed to discern the kinetics of the reaction by scrutinizing the concentration variations of pulegone and its resultant products, employing a reaction rate equation delineated as follows:

$$r = -\frac{dc}{dt} = k \times c^m \times p(H_2)^n = K \times C^{m1}$$ **.....Eq. S3**

$$lnKA = lnA - \frac{Ea}{RT}$$ **.....Eq. S4**

Here, r denotes the reaction rate, c signifies concentration, t represents time, m and n denote the reaction orders for pulegone and H_2, respectively, and k denotes the rate constant. K

symbolizes the rate constant in the simplified reaction rate equation, assuming a slight variation in (H_2) during the reaction as compared to the high pressure of H_2. Further, A represents the pre-exponential coefficient, Ea denotes the activation energy, R signifies the gas constant, and T represents temperature.

Kinetic and durability studies further validate the performance of the optimised 5%Si-Pd/C catalyst. Time-course experiments conducted at 313, 323, and 333 K (Fig. S8a) show an exponential decay in pulegone concentration, with all datasets fitting well to a pseudo-first-order kinetic model (Eq. S3 R^2 > 0.97). Increasing temperature accelerates pulegone consumption, consistent with a surface-controlled hydrogenation process. The Arrhenius plot of ln k versus 1/T (Eq. S4, Fig. S5b) yields an apparent activation energy of 37.89 kJ mol^{-1} (R^2 > 0.99; Table S8, ESI†), indicating efficient hydrogen activation at the Pd–Si interfacial sites under mild conditions.

To further probe the role of hydrogen, additional experiments were performed by systematically varying H_2 pressure (2-10 psi) at fixed temperature (50 °C) and reaction time (55 min). As shown in Fig. S8c, increasing H_2 pressure enhances the initial reaction rate and overall conversion, confirming that hydrogen availability directly influences the hydrogenation kinetics. This behaviour supports the pseudo-first-order treatment with respect to pulegone under fixed H_2 pressure conditions used for temperature-dependent kinetic analysis.

Catalyst stability (Fig. S8d) was evaluated over five consecutive cycles with intermediate filtration, washing, and regeneration at 650 °C. Both conversion and menthone/isomenthone selectivity remain largely preserved, with only ~4.5% activity loss after the fifth cycle, attributed to minor Pd sintering, thereby confirming excellent operational stability of the 5%Si-Pd/C catalyst.

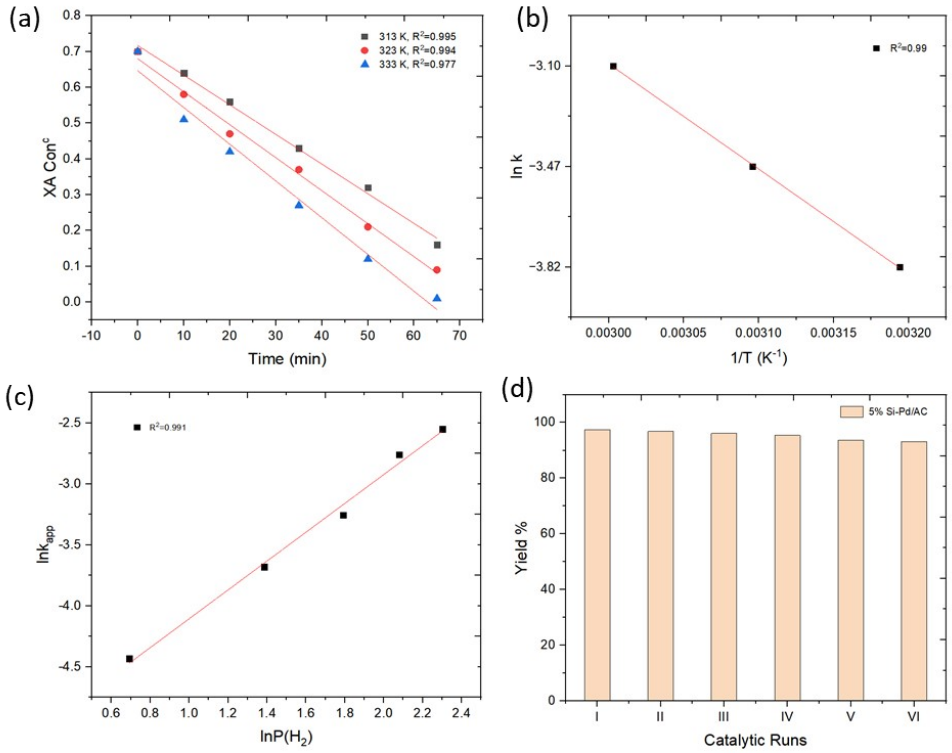

Fig. S8: Kinetic measurements and reusability test of 5%Si-Pd/C catalyst, (a) Initial rate Vs Reaction time; (b) Arrhenius correlation of ln K, (c) effect of varying pressure (d) performance plot.

Table S10. Catalytic activity of dehydrogenation/hydrogenation of pulegone using 5%Si-Pd/C catalysts.

Catalysts	**XA/time (min)[a]**	**RA0 (µmol/gcat·s)[b]**	**TOF_o [c] (s^{-1})**	**Ea (KJ/mol)**
5%Si-Pd/C	100/55	18.12	1.27	37.89

[a] Time when it reaches 100% conversion of pulegone, [b] Initial reaction rate, [c] Initial turnover frequency

11. Valorization of Pulegone containing essential oils

Table S11 summarises the compositional changes observed during the selective hydrogenation of pulegone in two industrially relevant multicomponent matrices-dementholised oil (DMO) and *CIM-Vishisht* essential oil-using the optimised 5%Si-Pd/C catalyst under mild conditions (10 psi H_2, 50 °C, 55 min, 10 wt% catalyst). These matrices differ markedly in both pulegone concentration and terpene complexity, providing a stringent assessment of catalyst tolerance towards co-existing components.

In DMO, which contains a relatively low pulegone content (2.8 wt%), hydrogenation results in efficient pulegone removal (to 0.5 wt%) with only marginal changes to the broader terpene

profile. The concentrations of menthone and isomenthone increase modestly (25.4 → 26.4 wt% and 17.7 → 18.7 wt%, respectively), consistent with selective conversion of pulegone without secondary hydrogenation or isomerisation of other monoterpenes. Importantly, structurally sensitive components such as (−)-menthol, menthylacetate, limonene, and α-pinene remain essentially unchanged, indicating that these co-existing terpenoids neither compete strongly for Pd active sites nor induce catalyst poisoning or inhibition.

In contrast, *CIM-Vishisht* essential oil represents an extreme case, containing a very high pulegone concentration (83.5 wt%). Under identical conditions, the catalyst achieves near-quantitative pulegone conversion (to 0.5 wt%), accompanied by a pronounced increase in menthone (3.5 → 42.0 wt%) and isomenthone (1.4 → 43.4 wt%). Despite the highly concentrated and compositionally dense matrix, no accumulation of over-hydrogenated products (e.g., menthol) or secondary side products is observed, and minor components (α-pinene, limonene, piperitenone, isopulegol) remain essentially unaffected.

The preservation of minor terpenoids and the absence of activity loss or selectivity drift demonstrate that the 5%Si-Pd/C catalyst is highly resistant to poisoning or competitive adsorption by oxygenated and olefinic impurities. This behaviour is attributed to Si-induced electronic modulation of Pd sites, which preferentially activates C=C bonds in pulegone while suppressing strong carbonyl anchoring and non-selective adsorption of other matrix components. Collectively, these results confirmed that the catalyst operates selectively and robustly in real essential-oil systems, validating its practical applicability for in-situ detoxification and upgrading of pulegone-rich industrial feed stocks.

Table S11. Composition of DMO, modified DMO, *CIM-Vishisht* essential oil and its modified oil.

Components	**DMO Oil**	**Modified DMO oil (5%Si-Pd/C)**	***CIM-Vishisht* essential oil**	**Modified *CIM-Vishisht* oil (5%Si-Pd/C)**
α-Pinene	0.5	0.4	0.7	0.6
Limonene	0.7	0.7	0.9	0.7
Menthone	25.4	26.4	3.5	42.0
Isomenthone	17.7	18.7	1.4	43.4
Isopulegol	1.2	1.0	1.4	1.4
Thymol	-	-	-	-
(-)-Menthol	24.9	24.5	2.5	2.1
Pulegone	2.8	0.5	83.5	0.5
Menthylacetate	9.4	8.8	0.9	0.7
Piperitenone	1.2	0.9	1.1	1.0
Total	83.8	81.9	95.9	92.4

Operating condition: H_2 (10 psi), 50 °C temperature, 55 min reaction time, 10 wt% catalyst loading.

12. Comparison with literature work

Table S12. Comparison of current procedure with previous literature reports.

Catalyst	Products	Selectivity[a]	Reaction conditions	Reference
Pt/SiO_2	Menthone/ Isomenthone	58	H_2 (10 bar), 115 °C, 12 h	Vetere et al. [1]
Fe/Ni		65	Electro catalytic hydrogenation	Lima et al. [2]
Pd/Al_2O_3				
		98.4	H_2 (40 bar) with CO_2+H_2 (160 bar), 2 h	Bogel-Lukasik, [3]
Ni-β-Cyclodextrin		98	H_2 (1.4 bar), 8 h	Ravi et al. [4]
5%Si-Pd/C		**98.6**	**H_2 (10 psi), 50 °C, 55 min**	**This work**

[a]= The product outcome is represented in terms of selectivity, which is calculated using equation, Selectivity%= Yield of desired product/ Conversion of reactant * 100.

As summarised in Table S12, several catalytic platforms have been explored for the selective hydrogenation of pulegone; however, each presents intrinsic limitations when evaluated against practical and scalable processing criteria. Vetere *et al.* reported Pt/SiO_2 catalysts affording only moderate menthone/isomenthone selectivity (58%) under relatively harsh conditions (115 °C, 10 bar H_2, 12 h), with substantial over-hydrogenation to menthol, indicating insufficient control over C=C versus C=O reduction pathways. Similarly, electrocatalytic hydrogenation using Fe/Ni cathodes (Lima *et al.*) achieved only ~65% selectivity and requires complex electrochemical setups, limiting throughput and industrial applicability.

Bogel-Łukasik *et al.* demonstrated excellent selectivity (98.4%) using Pd/Al_2O_3 in supercritical CO_2; however, this process necessitates extreme operating conditions (40 bar H_2 with total pressures exceeding 160 bar), specialised high-pressure equipment, and high energy input, rendering it economically and operationally prohibitive for large-scale deployment. In contrast, the Ni–β-cyclodextrin system reported by Ravi *et al.* achieves high selectivity (98%) at lower hydrogen pressure (1.4 bar), but requires prolonged reaction times (8 h) and relies on supramolecular host–guest interactions that are sensitive to solvent composition, moisture, and catalyst reuse, posing challenges for continuous operation and scale-up.

The 5%Si-Pd/C catalyst developed in this work overcomes these limitations by combining high selectivity (98.6%)**,** short reaction time (55 min**)**, and **v**ery mild hydrogen pressure (10 psi ≈ 0.69 bar) with a robust, recyclable heterogeneous catalyst architecture. Unlike prior systems,

the present catalyst operates efficiently in real essential-oil matrices, maintains activity over repeated cycles, and benefits from a clearly established structure–function relationship. Kinetic analysis and DFT calculations (in below section) demonstrated that Si incorporation electronically tunes Pd active sites, suppressing strong carbonyl adsorption while preserving olefin activation-an effect not accessible in conventional Pd, Pt, Ni, or supramolecular systems.

Overall, relative to reported heterogeneous, electrocatalytic, and supramolecular approaches, the Si-Pd/C catalyst provides the most balanced combination of mild conditions, rapid kinetics, operational robustness, and mechanistic clarity, establishing it as a technologically superior platform for selective pulegone detoxification and upgrading.

13. Computational details

All density functional theory (DFT) calculations were performed using the Vienna *ab initio* Simulation Package (VASP)*(5)*. The projector augmented wave (PAW)*(6)* method was employed, and the Perdew–Burke–Ernzerhof (PBE) exchange–correlation functional within the generalized gradient approximation (GGA)*(7)* was used throughout. Long-range dispersion interactions were accounted for using the DFT-D3*(8)* method of Grimme. Pd-C and Si-Pd-C surfaces were modelled using periodic slab geometries with vacuum separation of 20 Å, and all structures were fully relaxed until residual forces were below 0.03 eV $Å^{-1}$. A plane-wave kinetic energy cutoff of 600 eV was applied for all calculations. Spin polarization was included in all simulations to capture possible surface-induced magnetic effects. Brillouin zone integrations were performed using Monkhorst-Pack *k*-point meshes appropriate for surface calculations, and electronic convergence was achieved with an energy tolerance of 10^{-7} eV. To more accurately reflect experimental hydrogenation conditions conducted in ethanol, solvent effects were incorporated using the implicit solvation model implemented in VASP (VASPsol)*(5)*. Geometry optimizations and total-energy calculations were performed in a solvent to ensure thermodynamic consistency.

Adsorption energies (E_{ads}) were calculated according to

$$E_{ads} = E_{surface + adsorbate} - E_{surface} - E_{adsorbate}$$

Where $E_{surface + adsorbate}$, $E_{surface}$, and $E_{adsorbate}$ correspond to the total energies of the adsorbed system, the surface, and the isolated pulegone molecule, respectively. Electronic structure analysis was performed using projected density of states (PDOS). Charge transfer and interfacial electronic redistribution were analyzed using Bader charge analysis and charge-density-difference (CDD) calculations.

Observation:

Density functional theory (DFT) calculations were performed on model Pd-C and Si-Pd-C surfaces interacting with pulegone using ethanol as an implicit reaction medium to elucidate

how Si incorporation modifies the electronic structure of Pd and governs adsorption selectivity between C=C and C=O functionalities. The optimized structural models of the pristine Pd-C and Si-incorporated Pd-C surfaces are shown in **Fig. S9(a,b)**, presenting both top and side views. Inclusion of solvent effects moderately stabilizes polar adsorption geometries but preserves the relative adsorption hierarchy observed under gas-phase conditions.

Optimized adsorption geometries of pulegone on the pristine Pd-C surface are presented in **Fig. S10**, showing representative binding modes through the C=C bond (**Fig. S10a**) and the C=O group (**Fig. S10b**). Carbonyl adsorption results in a short Pd-O bond distance (2 Å), indicating a strong Pd-O interaction. In contrast, adsorption geometries on the Si-incorporated surface (**Fig. S11**) reveal a markedly different behavior. While C=C adsorption remains feasible on Si-Pd-C (**Fig. S11a**), C=O adsorption is significantly destabilized (**Fig. S11b**), with elongated Pd-O distances (2.23 Å) and reorientation of the pulegone molecule away from the Pd center. These structural trends directly suggest that Si incorporation suppresses strong carbonyl anchoring on Pd sites.

The energetic preference of adsorption modes is quantitatively summarized in **Fig. S12**, which compares adsorption energies for C=O and C=C binding on pristine and Si-modified surfaces. On pristine Pd-C surfaces, C=O adsorption strongly dominates over C=C binding (E_{ads}= -4.08 eV vs. -1.80 eV in gas phase), indicating a dominant Pd-O interaction. Upon inclusion of solvent effects (ethanol), the corresponding adsorption energies become -4.04 eV for C=O and -1.76 eV for C=C, demonstrating only a minor stabilization shift (~0.04 eV) while preserving the intrinsic adsorption hierarchy. PDOS analysis (**Fig. S13a-f**) reveals substantial O *p*-Pd *d* orbital overlap near the Fermi level (*E*_F), enabling strong Pd→π*(C=O) back-donation that stabilizes the adsorption geometry. This is quantitatively supported by Bader analysis (**Table S13**), which shows significant charge accumulation on Pd (+0.26 |e|) for C=O adsorption, compared to weaker charge transfer for C=C adsorption (+0.11 |e|). Corresponding CDD plots (**Fig. S14a**) display strong charge accumulation (yellow isosurfaces) at the Pd-O interface, confirming robust carbonyl anchoring and explaining the intrinsic tendency of Pd/C to promote C=O hydrogenation and over-reduction.

In contrast, incorporation of Si at the Pd-carbon interface fundamentally reshapes the adsorption landscape. On the Si-Pd-C surface, C=O adsorption becomes thermodynamically unfavourable (E_{ads}= +0.84 eV in gas phase), whereas olefinic adsorption remains mildly stabilized (-0.22 eV). Under solvent conditions, these values change only marginally to +0.80 eV for C=O and -0.19 eV for C=C, confirming that dielectric screening does not alter the adsorption selectivity trend. Surface DOS and PDOS analyses (**Fig. S13**) show that Si downshifts and depletes Pd d states near the Fermi level, suppressing Pd→π*(C=O) back-donation while retaining moderate Pd-π(C=C) interaction. Consistently, Bader analysis reveals substantial charge accumulation on Si for both adsorption modes (+0.61 |e| for C=O and +1.02 |e| for C=C) (**Table S13**), indicating that Si acts as an electron sink that withdraws charge from Pd. CDD plots (**Fig. S14b**) further demonstrate that, on Si-Pd-C, charge accumulation for

C=O adsorption is localized around Si-O motifs rather than Pd, evidencing electronic decoupling of the carbonyl group from Pd active sites. In contrast, moderate charge redistribution persists at the Pd-C interface for C=C adsorption, enabling selective C=C activation.

Importantly, the negligible variation in adsorption energies between gas and solvent phases (<0.05 eV across all configurations) indicates that the chemoselectivity originates from intrinsic electronic structure modulation induced by Si incorporation rather than solvent-mediated stabilization effects.

This comprehensive DFT analysis establishes Si as a selective electronic regulator that quenches Pd-carbonyl interactions while maintaining controlled Pd-olefin coupling. By inverting Pd's intrinsic C=O > C=C adsorption preference to C=C-selective binding, Si incorporation provides the atomic-level origin of Si-Pd-C's superior performance (97.6% menthone-isomenthone yield) versus unmodified Pd-C (55.2% selectivity).

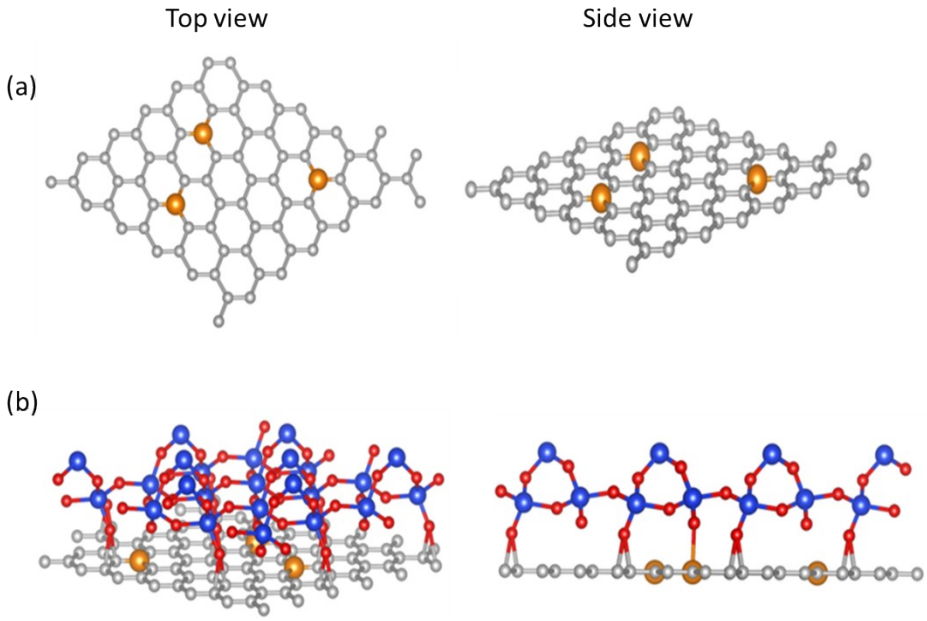

Fig. S9. Structural models of pristine and Si-modified Pd-C surfaces. Top and side views of (a) Pd-C and (b) Si-incorporated Pd-C surfaces. Colour code: C (grey), Pd (orange), Si (blue), O (red).

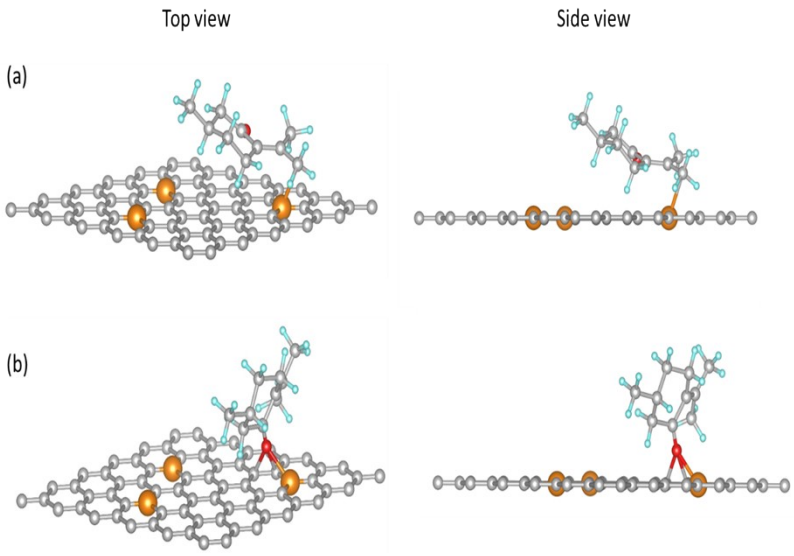

Fig. S10: DFT-optimized adsorption configurations of alkene and carbonyl-containing pulegone on Pd-C surfaces. Top and side views illustrating representative adsorption orientations of (top panels) (A) C=C interaction & (B) C=O interaction. Colour code: C (grey), Pd (orange), O (red), and H (cyan).

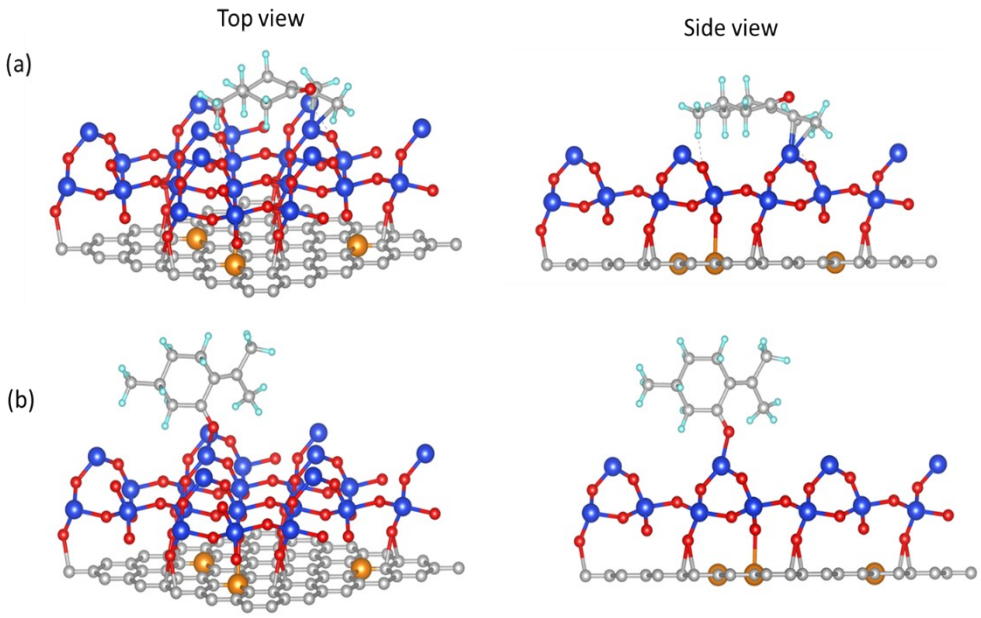

Fig. S11: DFT-optimized adsorption configurations of alkene and carbonyl-containing pulegone on Si-Pd-C surfaces. Top and side views illustrating representative adsorption orientations of (top panels) (A) C=C interaction & (B) C=O interaction. Colour code: C (grey), Pd (orange), Si (Blue), O (red), and H (cyan).

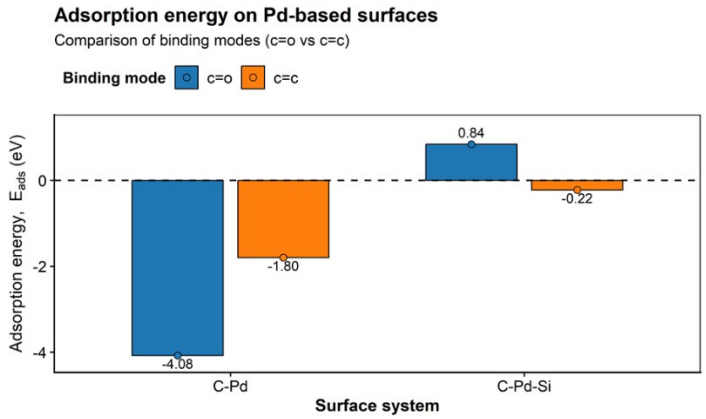

Fig. S12: Comparison of adsorption energies for C=O (orange) and C=C (blue) binding modes of pulegone on pristine Pd-C and Si-modified Pd-C surfaces.

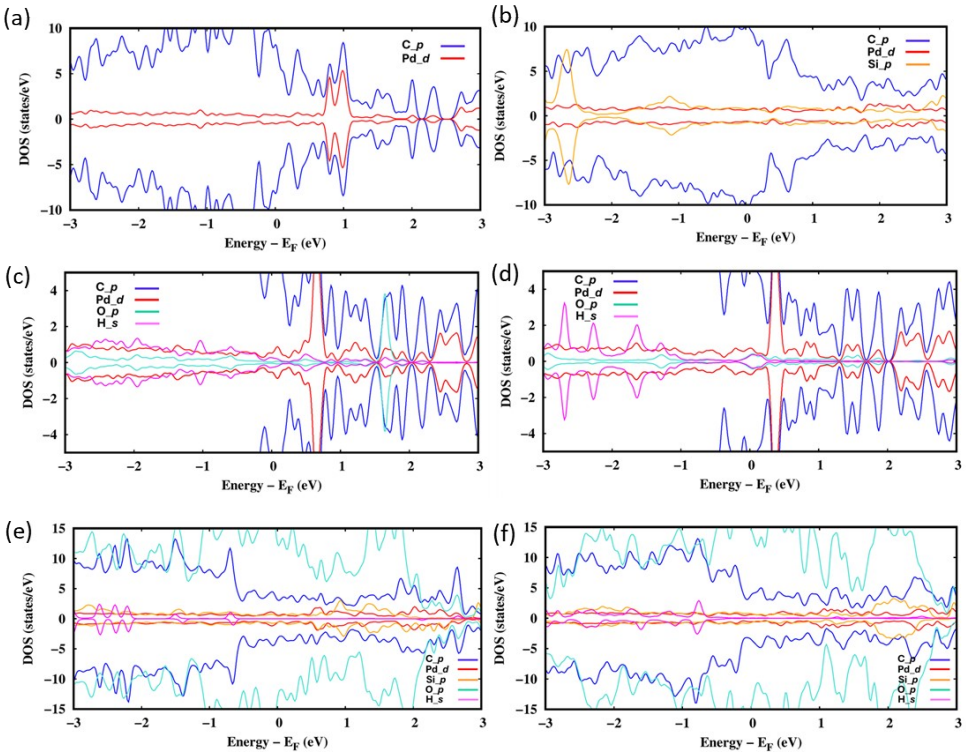

Fig. S13: Projected density of states (PDOS) of (a) Pd-C and (b) Si-Pd-C surfaces, and of pulegone adsorbed through C=O and C=C motifs on Pd-C [(c,d)] and Si-Pd-C [(e,f)], illustrating the influence of Si incorporation on electronic structure and adsorbate-surface interactions.

Table S13: *Bader analysis*

	Pd	**Si**
Pd-C-C=O	+0.26	
Pd-C-C=C	+0.11	

Si-Pd-C-C=O	+0.61
Si-Pd-C-C=C	+1.02

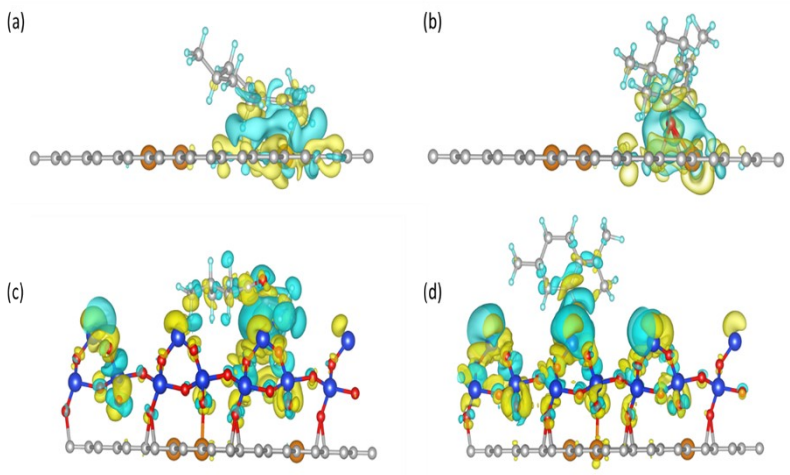

Fig. S14: Charge density difference (CDD) plots for pulegone adsorption on **Pd-C** surfaces showing (a) C=C and (b) C=O binding configurations, and on **Si-Pd-C** surfaces showing (c) C=C and (d) C=O binding configurations (isovalue = 0.01 e bohr^{-3}). Yellow and cyan isosurfaces represent charge accumulation and charge depletion, respectively.

References

1. V. Vetere, G. F. Santori, A. Moglioni, G. Y. Moltrasio Iglesias, M. L. Casella and O. A. Ferretti**, *Catal. Lett.***, 2002**, *84*, 251–257.**
2. M. V. Lima, F. D. Menezes, B. de Barros Neto and M. Navarro**, *J. Electroanal. Chem.***, 2008**, *613*, 58–66.**
3. E. Bogel-Łukasik**, *J. Supercrit. Fluids***, 2015**, *99*, 121–128.**
4. P. Ravi, R. Ravichandran and S. Divakar**, *J. Mol. Catal. A: Chem.***, 1999**, *148*, 145–155.**
5. Hafner, J. *Ab-initio* simulations of materials using VASP: Density-functional theory and beyond. *Journal of Computational Chemistry* **2008**, *29*(13), 2044–2078.
6. Blöchl, P. E. Projector augmented-wave method. *Physical Review B* **1994**, *50*(24), 17953–17979.
7. Perdew, J. P.; Burke, K.; Ernzerhof, M. Generalized Gradient Approximation Made Simple. *Physical Review Letters* **1996**, *77*(18), 3865–3868.
8. Goerigk, L. A Comprehensive Overview of the DFT-D3 London-Dispersion Correction. In *Non-Covalent Interactions in Quantum Chemistry and Physics*; Elsevier, 2017; pp 195–219.